Article

Two annual cycles of the Pacific cold tongue under orbital precession

https://doi.org/10.1038/s41586-022-05240-9

Received: 19 April 2022

Accepted: 16 August 2022

Published online: 9 November 2022

Check for updates

John C. H. Chiang[1,2]✉, Alyssa R. Atwood[3], Daniel J. Vimont[4], Paul A. Nicknish[5], William H. G. Roberts[6], Clay R. Tabor[7] & Anthony J. Broccoli[8]

The Pacific cold tongue annual cycle in sea surface temperature is presumed to be driven by Earth's axial tilt[1–5] (tilt effect), and thus its phasing should be fixed relative to the calendar. However, its phase and amplitude change dramatically and consistently under various configurations of orbital precession in several Earth System models. Here, we show that the cold tongue possesses another annual cycle driven by the variation in Earth–Sun distance (distance effect) from orbital eccentricity. As the two cycles possess slightly different periodicities[6], their interference results in a complex evolution of the net seasonality over a precession cycle. The amplitude from the distance effect increases linearly with eccentricity and is comparable to the amplitude from the tilt effect for the largest eccentricity values over the last million years (e value approximately 0.05)[7]. Mechanistically, the distance effect on the cold tongue arises through a seasonal longitudinal shift in the Walker circulation and subsequent annual wind forcing on the tropical Pacific dynamic ocean–atmosphere system. The finding calls for reassessment of current understanding of the Pacific cold tongue annual cycle and re-evaluation of tropical Pacific palaeoclimate records for annual cycle phase changes.

The Pacific cold tongue is an integral part of the tropical Pacific coupled ocean–atmosphere system and possesses a dominant annual cycle in sea surface temperature (SST) (Extended Data Fig. 1), even though insolation at the equator peaks twice a year[1](Extended Data Fig. 2a). Prevailing theory developed in the 1990s[1–5] explained the annual cycle through the following sequence: an annual mean equatorial cold tongue arises through easterly trade winds which shallow the thermocline to the east, allowing upwelling to bring cold water from below the thermocline into the mixed layer[8]. Because of the northward bias of the Pacific Intertropical Convergence Zone[9] southeasterly trade winds cross the equator throughout the year. Their strength changes over the course of a year, controlled by the differential heating between hemispheres resulting from the tilt effect, with a delay due to the thermal inertia of the ocean. The southeasterly trade winds are strongest in boreal autumn (Extended Data Fig. 1b) and cause surface waters to cool at the eastern boundary through coastal upwelling that propagates westwards along the equator, facilitated by zonal ocean–atmosphere feedback[10,11]; the same winds also drive increased surface heat fluxes and vertical mixing at the equator, further cooling the equatorial surface ocean[3,10]. Conversely, when the southeasterly trade winds weaken in boreal spring, the cold tongue is warmer (Extended Data Fig. 1c). Because the cold tongue annual cycle is controlled by the tilt effect, its phase relative to the calendar year should be relatively immutable as both are timed to the equinoxes.

This prevailing view was recently challenged by an Earth system model[12] (Geophysical Fluid Dynamics Laboratory (GFDL) CM 2.1; Methods) simulating a remarkable change in the phase of the cold tongue annual cycle with the longitude of perihelion (the position of perihelion relative to the moving vernal equinox as shown in Fig. 1; hereafter LOP). The eccentricity was set to 0.0493, being the maximum attained over the last 600,000 years[7] and about three times as large as the modern-day value (Extended Data Fig. 2b). When the LOP was altered from 90° (perihelion at winter solstice) to 180° (perihelion at vernal equinox), the coldest month changed from August to October; then to January for LOP at 270° (perihelion at summer solstice) and then to May for LOP at 0° (perihelion at autumnal equinox) (Fig. 2, top row). The amplitude of the annual cycle also changed dramatically, being largest for LOP at 90° and 180° and smallest with LOP at 0°, despite obliquity being fixed. No straightforward relationship is discernible when the cold tongue annual cycle behaviour is compared with its corresponding seasonal cycle of insolation at the equator (Extended Data Fig. 2c–f). Similar cold tongue behaviour is found in identical sets of simulations performed with two other Earth System models (iCESM 1.2 and HadCM3) (Fig. 2, second and third rows, respectively) and with a fourth model (EC Earth; Extended Data Fig. 3) performed with slightly different orbital parameters (Methods section on 'Earth System Model simulations').

[1]Department of Geography, University of California, Berkeley, CA, USA. [2]Research Institute for Environmental Changes, Academia Sinica, Taipei, Taiwan ROC. [3]Department of Earth, Ocean, and Atmospheric Sciences, Florida State University, Tallahassee, FL, USA. [4]Department of Atmospheric and Oceanic Sciences, University of Wisconsin-Madison, Madison, Madison, WI, USA. [5]Department of Earth and Planetary Science, University of California, Berkeley, CA, USA. [6]Department of Geography and Environmental Science, Northumbria University, Newcastle-upon-Tyne, UK. [7]Department of Geosciences, University of Connecticut, Storrs, CT, USA. [8]Department of Environmental Sciences, Rutgers University, New Brunswick, NJ, USA. ✉e-mail: jch_chiang@berkeley.edu

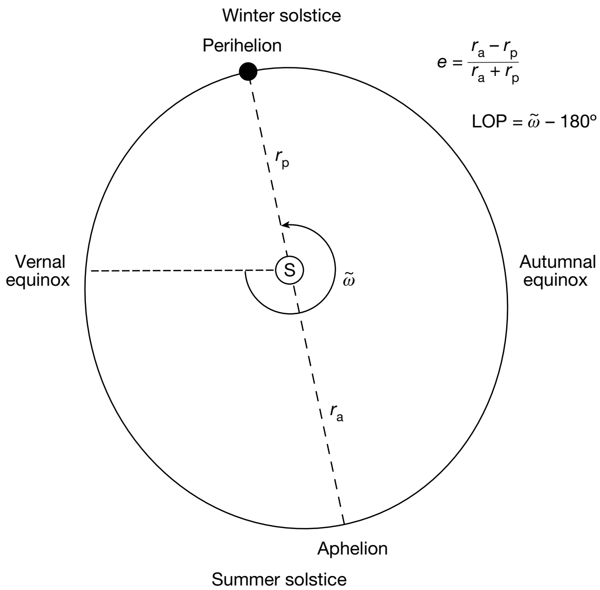

Fig. 1 | Schematic of the Earth's orbital configuration. The Earth's orbit around the Sun (marked S) is elliptical with the Sun at one focal point and with the closest approach at perihelion (at a distance r_p) and furthest at aphelion (r_a). The direction of the orbit is counterclockwise. The eccentricity e, defined in the figure, measures how elliptical the orbit is: $e = 0.0493$ is used for the simulations reported in Fig. 2, about three times larger than the modern-day value. The equinox and solstice points are named following Northern hemisphere seasons. The LOP relative to the moving vernal equinox is defined (following Fig. 8 of ref. [38]) as the angular distance from vernal equinox to perihelion following Earth's orbit ($\tilde{\omega}$, in degrees), subtracted by 180°. Thus, LOP is 90° and 180° if perihelion occurs during winter solstice and vernal equinox, respectively. Perihelion, as drawn in the schematic, is positioned for modern day, with an LOP of about 103° and date of around 3 January. Because the distance effect annual cycle (from perihelion to perihelion, otherwise called the anomalistic year, 365.259636 d (ref. [6])) is slightly longer than the tilt effect annual cycle (from equinox to equinox, otherwise known as the tropical year, 365.242189 d (ref. [6])), the LOP increases over time. A complete revolution of the LOP is the precession cycle, about 22,000 yr (ref. [38]). Note that the Gregorian calendar is referenced to the vernal equinox, with its rule for leap days designed to resynchronize the calendar year with the tropical year.

Cold tongue response to eccentricity

When eccentricity is set to zero and annual cycle forcing arises solely from the tilt effect, the simulated Pacific cold tongue seasonality behaves in a way that is consistent with prevailing theory, with the cold peak timed to boreal autumn and warm peak to boreal spring (Fig. 2, last column). We show that as orbital eccentricity is introduced, another cold tongue annual cycle emerges. Simulations with an Earth system model (Community Earth System Model (CESM) 1.2; Methods section on 'Earth System Model simulations) spanning the range of LOP are undertaken at three eccentricities (e)—0.01, 0.02 and 0.04—covering the typical range over the last million years[7] (hereafter the CESM LOP simulations; Methods section on 'Earth System Model simulations). All other boundary conditions are set to pre-industrial levels (1850 AD), including obliquity.

The cold tongue annual cycle shows two distinct features as the longitude of perihelion is varied (Fig. 3a; for $e = 0.04$): a change in the timing of peaks and troughs and a marked reduction in amplitude near LOP = 0°. We fit the results of Fig. 3a with the sum of two cosines, one whose phase is fixed to the calendar representing the tilt effect and the other whose phase changes linearly with the LOP representing the distance effect. We also include a semi-annual cycle with its phase fixed to the calendar, to account for insolation peaking at the equator twice a year during the equinoxes (Extended Data Fig. 2a).

$$\mathrm{CT_{fit}} = A_\mathrm{T}\cos\left(\left(\frac{2\pi}{12}\right)(m-p_\mathrm{T})\right) + A_\mathrm{D}\cos\left(\left(\frac{2\pi}{12}\right)(m-p_\mathrm{D}) - \left(\frac{\mathrm{LOP}\pi}{180}\right)\right) + A_\mathrm{S}\cos\left(\left(\frac{2\pi}{6}\right)(m-p_\mathrm{S})\right) \quad (1)$$

in which $\mathrm{CT_{fit}}$ is the modelled cold tongue sea surface temperature (with annual cycle removed), A_T and p_T are the amplitude and phase of the annual cycle for the tilt effect, A_D and p_D for the distance effect and A_S and p_S for the semi-annual cycle. Parameter m is the numerical months of the year from 0 to 12 (with 0.5 corresponding to mid-January) and LOP is in degrees.

The best-fit surface to the data (Fig. 3b; Methods section on 'Surface fitting') captures its salient features, including the change in phase and reduction in amplitude near LOP = 0°. The tilt and distance annual cycles are comparable in amplitude (Fig. 3d,e) but the semi-annual contribution is relatively small (Fig. 3f). The same fitting exercise but with $e = 0.01$ and 0.02 (Extended Data Fig. 4) shows an essentially unchanged annual cycle contribution from the tilt effect and semi-annual cycle (Table 1) but the amplitude of the distance effect annual cycle decreases linearly with decreasing eccentricity (Fig. 3c). A similar outcome occurs when fitting equation (1) to a simulation with $e = 0$ (the tilt-only run), assuming $A_\mathrm{D} = 0$ (Table 1). The consistency in the fitted parameters lends confidence to the validity of our model.

The above results are consistent with cold tongue seasonality arising from the sum of the tilt and distance effect annual cycles. As the duration of the distance effect annual cycle is slightly longer than that of the tilt effect (at present by about 25 min)[6], the two interfere resulting in a complex evolution of the net cold tongue annual cycle with orbital precession. The amplitude from the distance effect increases linearly at around 0.23 K per 0.01 eccentricity units (Fig. 3c), meaning that even at today's low eccentricity the amplitude from the distance effect is about one-third of that from the tilt effect. For the largest orbital eccentricities over the last million years ($e > 0.05$) (ref. [7]), the distance effect amplitude is as large or even larger than the tilt effect amplitude.

We confirm this interpretation through a simulation that removes the tilt effect by setting obliquity to 0° (the distance-only run); we use $e = 0.05$ (and LOP = 0°) such that the distance effect amplitude approximately matches the tilt effect amplitude. In contrast to the annual cycle in the tilt-only run (Extended Data Fig. 5c), the distance-only run shows an annual cycle with a cold peak in early May and warm peak in mid-late October (Extended Data Fig. 5b). When the two annual cycles are summed, they produce a cold tongue seasonality which resembles the simulation with both distance and tilt effects present (Extended Data Fig. 5a,d). With both eccentricity and obliquity set to zero (the zero annual forcing run), the cold tongue annual cycle essentially disappears (Extended Data Fig. 5e).

Equatorial wind and thermocline changes

Previous model studies using mid-Holocene orbital conditions (corresponding to LOP of about 0°)[12–14] have suggested that the cold tongue annual cycle changes are dynamically induced through equatorial thermocline changes. Ref. [12] shows in a LOP = 0° simulation that, in boreal spring, weakening trade winds in the western equatorial Pacific coincide with a deeper equatorial thermocline, the last of which propagates eastwards to warm the eastern equatorial SST by boreal autumn. Thermodynamic SST changes by direct insolation forcing also contribute to the autumn warming. The opposite occurs for the other half of the year. We note that the prevailing theory for the cold tongue annual cycle does not prescribe a role to seasonal variations in the thermocline[2].

We similarly examine equatorial wind stress and thermocline changes in the CESM LOP simulations. Using the $e = 0.04$ case, we find a clear eastward propagation of the thermocline anomaly originating from

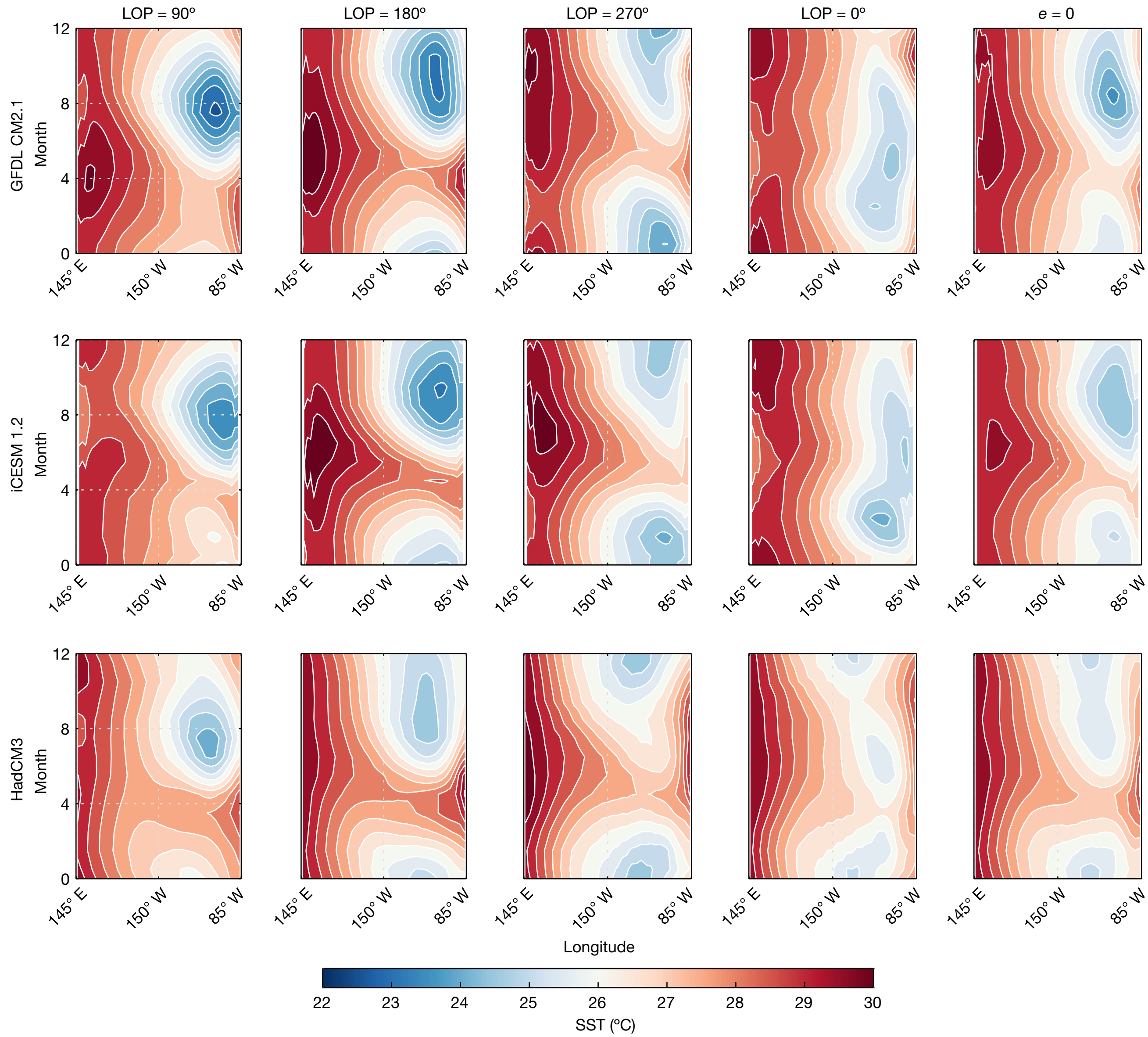

Fig. 2 | Annual cycles of equatorial Pacific SSTs for three different Earth System models show a remarkable and consistent seasonal variation with the LOP. Plotted is the climatological monthly mean SST averaged over 6° S–6° N, for GFDL CM 2.1 (ref. [12]) (top row), iCESM 1.2 (ref. [40]) (second row) and HadCM3 (third row). The numbers on the top row denote the LOP (for which 90° is perihelion at winter solstice, 180° at vernal equinox, 270° at summer solstice and 0° at autumnal equinox). The last column ($e = 0$) denotes simulations with eccentricity set to zero. To facilitate comparison, an offset is added to each panel so that the annual mean SST averaged over 145° E–85° W is the same as for the observational data, as shown in Extended Data Fig. 1a, 27.44 °C. Note that the time (y) axis here and in other figures is such that 0 is the start of the year and 12 is the end; mid-January is thus 0.5.

the western Pacific for all LOP cases, provided that the tilt effect contribution is removed beforehand (Extended Data Fig. 6, contours). Zonal wind stress changes in the western equatorial Pacific precede thermocline anomalies for all LOP cases, with anomalous westerlies corresponding to a deeper thermocline and vice versa (Extended Data Fig. 6, shaded). Thus, the distance effect annual cycle seems to involve the same coupled ocean–atmosphere dynamics and equatorial thermocline propagation that gives rise to the El Nino/Southern Oscillation (ENSO)[15].

We confirm this interpretation using a set of simplified model simulations (Methods section on 'Simulations with an ICM of the tropical Pacific'). First, we obtain the distance effect wind response by imposing the appropriate orbital conditions (and LOP = 0°) in CESM 1.2 with the ocean component replaced by a 'slab' ocean that incorporates thermodynamic ocean–atmosphere interactions from surface fluxes but not the dynamical thermocline evolution. They generate a seasonal cycle of zonal wind anomalies in the equatorial western Pacific that is independent of the dynamic ocean–atmosphere coupling, with peak anomalous westerlies occurring at the end of April (Extended Data Fig. 7a). These winds are then imposed as an annually repeating forcing on an intermediate coupled model[16] (ICM) which contains the essential dynamics to simulate the ENSO. The ICM responds by producing a cold tongue annual cycle with the peak warm phase occurring 3–4 months after the peak anomalous westerlies in the western Pacific (Extended Data Fig. 7a). As in the CESM LOP simulations, eastward-propagating thermocline variations link the zonal wind annual cycle in the western Pacific to the annual cycle of the cold tongue in the ICM (Extended Data Fig. 7b). We conclude that the coupled dynamics that generate

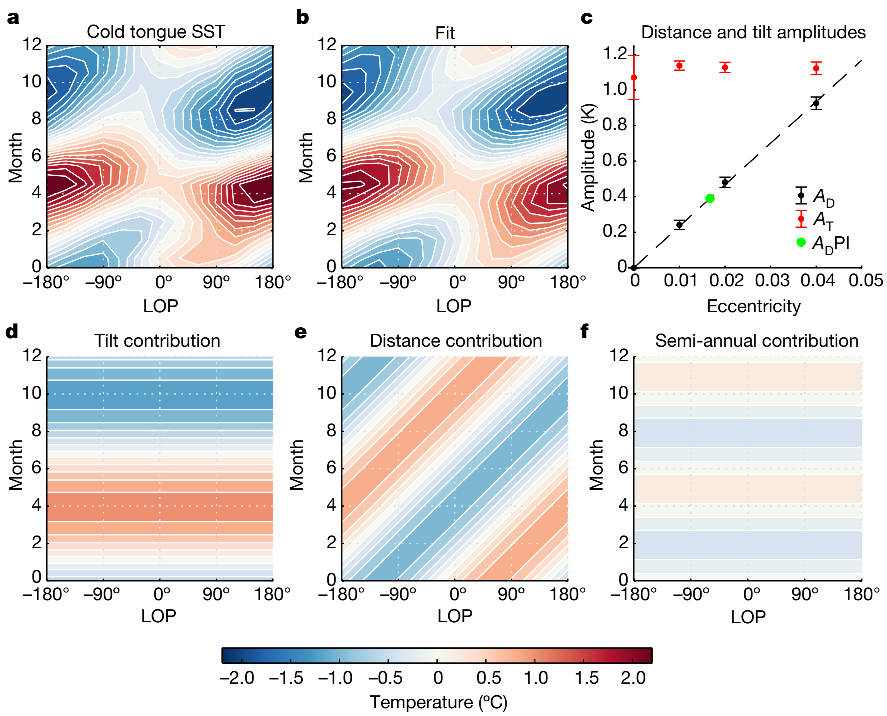

Fig. 3 | Variation of the cold tongue annual cycle to LOP arises from the sum of the tilt and distance effect contributions. **a**, Cold tongue SST (averaged over 6° S–6° N, 140–90° W) annual cycle for $e = 0.04$ with varying longitude of perihelion. The annual mean is removed from each annual cycle before plotting. **b**, Least-square surface fit of the data in **a**, using equation (1). **c**, Fitted coefficients of the distance effect amplitude (A_D, black symbols) and the least-square linear fit to the data forced through the intercept (dashed line). The bars indicate the 95% confidence bounds for each A_D fit. For comparison, the fitted coefficients of the tilt effect amplitude (A_T) are shown in red. The green dot indicates the distance effect amplitude for eccentricity at pre-industrial (PI) level ($e = 0.0167$). **d**–**f**, Contributions of the fit in **b** from tilt effect (**d**), distance effect (**e**) and semi-annual cycle (**f**). The same colour scale is used for **a**, **b**, **d**, **e** and **f**.

ENSO are also integral to the distance effect cold tongue annual cycle. These coupled dynamics arise as a forced response to the annual cycle in zonal wind stress changes in the western Pacific which arise from a thermodynamic response to the distance effect.

The peak warm phase of the cold tongue in the distance-only run occurs 4–5 months after the peak anomalous westerlies (Extended Data Fig. 5b), a longer lag time than in the ICM (Extended Data Fig. 7a). We attribute this difference to the direct thermodynamic response of the distance effect insolation on SST, which has its peak warm phase about 7 months after the peak westerlies (Extended Data Fig. 7c); this would act to delay the timing of the warm peak in the cold tongue.

Table 1 | Fitted coefficients for equation (1) to the cold tongue SST annual cycle variation with LOP in the CESM LOP simulations, for various eccentricity values

Eccentricity (e)	A_T (K)	p_T (month)	A_D (K)	p_D (month)	A_S (K)	p_S (month)
0.00	1.07 (0.95, 1.19)	4.02 (3.80, 4.25)	0	-	0.33 (0.21, 0.46)	5.07 (4.71, 5.42)
0.01	1.14 (1.11, 1.16)	4.03 (3.99, 4.08)	0.24 (0.22, 0.27)	10.13 (9.92, 10.33)	0.31 (0.29, 0.34)	5.00 (4.92, 5.08)
0.02	1.13 (1.10, 1.16)	4.01 (3.96, 4.06)	0.48 (0.45, 0.51)	10.08 (9.97, 10.20)	0.32 (0.29, 0.35)	4.98 (4.90, 5.07)
0.04	1.12 (1.09, 1.16)	3.94 (3.88, 4.00)	0.93 (0.89, 0.96)	10.02 (9.95, 10.10)	0.32 (0.29, 0.36)	4.90 (4.79, 5.00)

The cold tongue SST is averaged over 140–90° W, 6° S–6° N. For zero eccentricity, A_D is assumed to be zero. The values in brackets indicate the 95% confidence bounds. Note the consistency in the coefficients for A_T, A_S, p_T, p_S and p_D across various eccentricities.

Zonal shift in the Walker circulation

The western Pacific wind changes result from a seasonal cycle in the longitudinal position of the Walker circulation driven by the distance effect. In the distance-only run, the equatorial easterlies in the western Pacific exhibit an annual cycle and essentially vanish between March and June (Fig. 4a, black contours). This feature contrasts with the zero annual forcing run in which the equatorial Pacific zonal winds are always easterly. The cold tongue is at its coldest (Fig. 4a, shaded) when the easterlies vanish, indicating that the winds are not being driven by the cold tongue SST. Rather, the vanishing easterlies result from an eastward shift of the main uplift region of the Walker circulation (Extended Data Fig. 8c), accompanied by an increase in the precipitation over the equatorial western Pacific and decrease over the Maritime Continent (Extended Data Fig. 8a). The opposite occurs during September–December (Extended Data Fig. 8b,d).

We use an atmospheric energy flux analysis[17] to confirm the Walker circulation shift and diagnose its causes (Methods section on 'Atmospheric energy flux analysis'). This analysis links the longitude of its main uplift region to the position of zero and diverging zonal energy flux, otherwise known as the energy flux prime meridian (EFPM). For the zero annual forcing run, the EFPM over the equatorial western Pacific stays at about 150° E throughout the year (Fig. 4a, green dashed line). With eccentricity increased to 0.05, a distance effect annual cycle in the EFPM emerges with an eastward shift between March and June following aphelion and a westward shift between September and December following perihelion (Fig. 4a, green solid line); note that it aligns

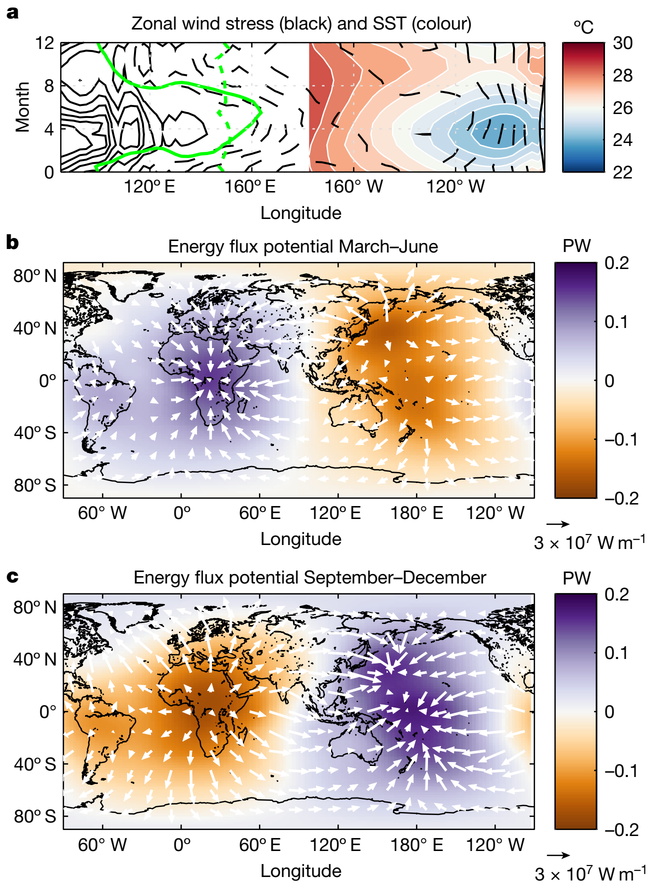

Fig. 4 | The distance effect on the longitude position of the Walker circulation as diagnosed by the energy flux potential. a, Equatorial Pacific zonal wind stress (black contours, contour interval 1×10^{-2} N m^{-2}; dashed contours are negative and zero contour not shown) and SST (shaded) averaged over 6° S–6° N for the distance-only run (obliquity = 0°, e = 0.05, LOP = 0°). Positive values of wind stress correspond to westerly winds. Because the focus is on the cold tongue, SST is only shown east of the date line; also, an offset is added so that the annual mean SST averaged over 145° E–85° W is the same as for the observational data, as shown in Extended Data Fig. 1a, 27.44 °C. The solid green line shows the EFPM over the western Pacific for the distance-only run and the dashed green line for the zero annual forcing run. **b**, Energy flux potential (shaded, units are petawatts (PW)) averaged over March–June, for the difference between the distance-only and zero annual forcing runs (the former minus the latter). The vectors correspond to the difference in the divergent horizontal atmospheric energy transport. **c**, Same as **b** but for September–December. See Methods section on 'Atmospheric energy flux analysis' for details on the calculations. The M_Map package[41] was used to generate the maps in **b** and **c**, using coastline data from the global self-consistent, hierarchical, high-resolution geography database[42].

well with the zonal wind stress changes over the western equatorial Pacific. The EFPM change is caused by a zonal dipole in the energy flux potential (Fig. 4b,c, shading) between the hemisphere extending from the Maritime Continent through the Pacific (the marine hemisphere, being mostly ocean), with the hemisphere extending from South America through to the Indian Ocean (the continental hemisphere, having relatively more land). For March–June following aphelion, there is increased zonal atmospheric energy transport from the marine to the continental hemisphere (Fig. 4b, vectors) and the EFPM (and hence the Walker uplift region) shifts eastwards. The opposite occurs in September–December following perihelion (Fig. 4c). Other diagnostics of the large-scale atmospheric circulation—upper tropospheric velocity potential and surface pressure—confirm the seasonal zonal shift in the Walker circulation and the global east–west hemispheric nature of its origins (Extended Data Fig. 8e–h).

The zonal energy transport arises from the differing thermal response of the two hemispheres to the distance effect. For September–December following perihelion, the surface of the marine hemisphere absorbs relatively more of the increased sunlight than that of the continental hemisphere, implying that the marine hemisphere fluxes less energy into the overlying atmosphere than the continental hemisphere. Because tropical atmospheric dynamics act to rapidly homogenize tropospheric temperature differences[18], there is increased zonal atmospheric energy transport from the continental to the marine hemisphere and the Walker circulation shifts to the west. The opposite occurs in March–June following aphelion. This behaviour is analogous to the latitudinal migration of the Intertropical Convergence Zone in response to atmospheric energy transport changes between the northern and southern hemispheres from the tilt effect[19,20].

Implications

Our findings call for a re-evaluation of mechanisms underpinning the Pacific cold tongue annual cycle, in particular thermocline changes. The distance effect may have escaped attention as the current annual cycle resembles that from the tilt effect alone and thus does not pose a challenge to the prevailing theory. It also begs the question: to what extent does the distance effect contribute to the seasonal cycle of other regional climates? This question is rarely asked[21] but this study demonstrates how new insights about the Earth's seasonal cycle are made possible if the tilt and distance effects are considered separately.

We also argue for a re-examination of tropical Pacific palaeoclimate records for changes to the annual cycle. Palaeoclimate studies examining tropical Pacific records on orbital timescales have largely framed cold tongue changes in terms of ENSO[22–27], although attempts have been made to separate amplitude changes into ENSO and annual cycle contributions[25,28–30]. Determining the phasing of palaeoproxy signals relative to the calendar year is more challenging and we are not aware of any attempts in this regard. It requires records that resolve the annual cycle and a marker to affix the calendar. The semi-annual cycle can potentially serve as a marker, as it is timed to equinoxes. We also note that a change in the cold tongue annual cycle may itself cause changes to ENSO because feedbacks that govern the latter depend on the seasonal cycle[31,32].

Finally, we speculate on the implications to the global palaeoclimate. The tropical Pacific is thought to play a defining role in palaeoclimate on orbital timescales[33,34], given its responsiveness to forcing and global reach through teleconnections. The phase of precession has been linked to many regional palaeoclimate changes around the globe, prominent examples being peak monsoon intensity[35,36] and the timing of the Ice Ages[37–39]. The implicit assumption is that the precession influence works through direct insolation changes at the latitude of the regional climate. However, our results indicate that the tropical Pacific may also be capable of remotely orchestrating precession changes around the globe, through altering the cold tongue annual cycle.

Online content

Any methods, additional references, Nature Research reporting summaries, source data, extended data, supplementary information, acknowledgements, peer review information; details of author contributions and competing interests; and statements of data and code availability are available at https://doi.org/10.1038/s41586-022-05240-9.

1. Mitchell, T. P. & Wallace, J. M. The annual cycle in equatorial convection and sea-surface temperature. *J. Clim.* **5**, 1140–1156 (1992).
2. Xie, S. P. On the genesis of the equatorial annual cycle. *J. Clim.* **7**, 2008–2013 (1994).
3. Chang, P. The role of the dynamic ocean–atmosphere interactions in the tropical seasonal cycle. *J. Clim.* **9**, 2973–2985 (1996).

4. Li, T. M. & Philander, S. G. H. On the annual cycle of the eastern equatorial Pacific. *J. Clim.* **9**, 2986–2998 (1996).
5. Wang, B. On the annual cycle in the Tropical Eastern Central Pacific. *J. Clim.* **7**, 1926–1942 (1994).
6. United States Nautical Almanac Office, United States Naval Observatory, Her Majesty's Nautical Almanac Office and the United Kingdom Hydrographic Office. *The Astronomical Almanac for the Year 2019* (United States Government Printing Office, 2019).
7. Berger, A. & Loutre, M. F. Insolation values for the climate of the last 10000000 years. *Quat. Sci. Rev.* **10**, 297–317 (1991).
8. Xie, S. P. & Philander, S. G. H. A. Coupled ocean–atmosphere model of relevance to the ITCZ in the Eastern Pacific. *Tellus* **46**, 340–350 (1994).
9. Philander, S. G. H. et al. Why the ITCZ is mostly north of the equator. *J. Clim.* **9**, 2958–2972 (1996).
10. Xie, S. P. Westward propagation of latitudinal asymmetry in a coupled ocean–atmosphere model. *J. Atmos. Sci.* **53**, 3236–3250 (1996).
11. Nigam, S. & Chao, Y. Evolution dynamics of tropical ocean–atmosphere annual cycle variability. *J. Clim.* **9**, 3187–3205 (1996).
12. Erb, M. P. et al. Response of the equatorial Pacific seasonal cycle to orbital forcing. *J. Clim.* **28**, 9258–9276 (2015).
13. Luan, Y., Braconnot, P., Yu, Y., Zheng, W. & Marti, O. Early and mid-Holocene climate in the tropical Pacific: seasonal cycle and interannual variability induced by insolation changes. *Clim. Past* **8**, 1093–1108 (2012).
14. Karamperidou, C., Di Nezio, P. N., Timmermann, A., Jin, F. F. & Cobb, K. M. The response of ENSO flavors to mid-Holocene climate: implications for proxy interpretation. *Paleoceanography* **30**, 527–547 (2015).
15. Neelin, J. D. et al. ENSO theory. *J. Geophys. Res.* **103**, 14261–14290 (1998).
16. Battisti, D. S. Dynamics and thermodynamics of a warming event in a coupled tropical atmosphere ocean model. *J. Atmos. Sci.* **45**, 2889–2919 (1988).
17. Boos, W. R. & Korty, R. L. Regional energy budget control of the intertropical convergence zone and application to mid-Holocene rainfall. *Nat. Geosci.* **9**, 892–897 (2016).
18. Sobel, A. H., Nilsson, J. & Polvani, L. M. The weak temperature gradient approximation and balanced tropical moisture waves. *J. Atmos. Sci.* **58**, 3650–3665 (2001).
19. Kang, S. M., Held, I. M., Frierson, D. M. W. & Zhao, M. The response of the ITCZ to extratropical thermal forcing: idealized slab-ocean experiments with a GCM. *J. Clim.* **21**, 3521–3532 (2008).
20. Chiang, J. C. H. & Friedman, A. R. Extratropical cooling, interhemispheric thermal gradients, and tropical climate change. *Ann. Rev. Earth Planet. Sci.* **40**, 383–412 (2012).
21. Thomson, D. J. The seasons, global temperature, and precession. *Science* **268**, 59–68 (1995).
22. Koutavas, A., Demenocal, P. B., Olive, G. C. & Lynch-Stieglitz, J. Mid-Holocene El Nino-Southern Oscillation (ENSO) attenuation revealed by individual foraminifera in eastern tropical Pacific sediments. *Geology* **34**, 993–996 (2006).
23. Cobb, K. M. et al. Highly variable El Nino-Southern Oscillation throughout the Holocene. *Science* **339**, 67–70 (2013).
24. Carre, M. et al. Holocene history of ENSO variance and asymmetry in the eastern tropical Pacific. *Science* **345**, 1045–1048 (2014).
25. Emile-Geay, J. et al. Links between tropical Pacific seasonal, interannual and orbital variability during the Holocene. *Nat. Geosci.* **9**, 168–173 (2016).
26. Thompson, D. M. et al. Tropical Pacific climate variability over the last 6000 years as recorded in Bainbridge Crater Lake, Galapagos. *Paleoceanography* **32**, 903–922 (2017).
27. White, S. M., Ravelo, A. C. & Polissar, P. J. Dampened El Nino in the Early and Mid-Holocene due to insolation-forced warming/deepening of the thermocline. *Geophys. Res. Lett.* **45**, 316–326 (2018).
28. Koutavas, A. & Joanides, S. El Nino-Southern Oscillation extrema in the Holocene and Last Glacial Maximum. *Paleoceanography* https://doi.org/10.1029/2012pa002378 (2012).
29. Thirumalai, K., Partin, J. W., Jackson, C. S. & Quinn, T. M. Statistical constraints on El Nino Southern Oscillation reconstructions using individual foraminifera: a sensitivity analysis. *Paleoceanography* **28**, 401–412 (2013).
30. Zhu, J. et al. Reduced ENSO variability at the LGM revealed by an isotope-enabled Earth system model. *Geophys. Res. Lett.* **44**, 6984–6992 (2017).
31. Battisti, D. S. & Hirst, A. C. Interannual variability in a tropical atmosphere ocean model—influence of the basic state, ocean geometry and nonlinearity. *J. Atmos. Sci.* **46**, 1687–1712 (1989).
32. Tziperman, E., Zebiak, S. E. & Cane, M. A. Mechanisms of seasonal–ENSO interaction. *J. Atmos. Sci.* **54**, 61–71 (1997).
33. Cane, M. A. A role for the Tropical Pacific. *Science* **282**, 59–61 (1998).
34. Chiang, J. C. H. The tropics in paleoclimate. *Ann. Rev. Earth Planet. Sci.* **37**, 263–297 (2009).
35. Prell, W. L. & Kutzbach, J. E. Monsoon variability over the past 150,000 years. *J. Geophys. Res.* **92**, 8411–8425 (1987).
36. Wang, Y. J. et al. Millennial- and orbital-scale changes in the East Asian monsoon over the past 224,000 years. *Nature* **451**, 1090–1093 (2008).
37. Hays, J. D., Imbrie, J. & Shackleton, N. J. Variations in Earths orbit—pacemaker of Ice Ages. *Science* **194**, 1121–1132 (1976).
38. Berger, A. Milankovitch theory and climate. *Rev. Geophys.* **26**, 624–657 (1988).
39. Cheng, H. et al. Ice Age terminations. *Science* **326**, 248–252 (2009).
40. Tabor, C. R. et al. Interpreting precession-driven delta O-18 variability in the South Asian monsoon region. *J. Geophys. Res.* **123**, 5927–5946 (2018).
41. Pawlowicz, R. M_Map: A mapping package for MATLAB, version 1.4m (UBC EOAS, 2020); www.eoas.ubc.ca/~rich/map.html
42. Wessel, P. & Smith, W. H. F. A global, self-consistent, hierarchical, high-resolution shoreline database. *J. Geophys. Res.* **101**, 8741–8743 (1996).